Research Article

# Development of multilayer PVA-MMT and PVA-CS film structures by spin coating-assisted layer-by-layer technique: Effect of PVA, CS and MMT nanoclay orientation on oxygen barrier properties

**Mbogniane Diouf[1,2], Frej Mighri[1,2*], Said Elkoun[1,3]**

[1]Research center for high performance polymer and composite systems, CREPEC, Montreal, Qc, Canada
[2]Department of Chemical Engineering, Laval University, Quebec, Qc, Canada, G1V 0A6
[3]Department of Mechanical Engineering, Université de Sherbrooke, QC, Canada, J1K 2R1
E-mail: Frej.mighri@gch.ulaval.ca

**Abstract:** The orientation of biopolymer macromolecules and nanoclay, specifically Montmorillonite (MMT) nanoplatelets, plays a crucial role in controlling the properties of multi-layer film structures. Understanding the impact of macromolecule and nanoclay platelets' orientation on barrier properties of packaging films is essential. To investigate the influence of hydrogen bonding in multilayer films structures, two polymers, namely polyvinyl alcohol (PVA) and chitosan (CS), were selected and laminated nanocomposite films were fabricated using the spin coating-assisted layer-by-layer (Spin-LbL) assembly technique. This technique facilitates the production of highly oriented nanocomposite films, where polymer chains and nanoclay particles align parallel to the film surface. Multi-directional 2-D wide-angle X-ray diffraction (2D-WADX) was successfully used to accurately assess the orientation and distribution of MMT nanoplatelets. Additionally, the films underwent characterization using X-ray diffraction (XRD) and Fourier transform infrared spectroscopy (FTIR). The 2D-WADX analysis revealed a parallel alignment of both the PVA chains and MMT clay nanoplatelets parallel to film surface. The XRD results confirmed the formation of intercalated nanolaminate structures, hydrogen-bonding interactions, and adjustments in the crystalline structure of PVA matrix. Through contact angle and oxygen permeability measurements, we observed that all quadri-layer film structures exhibited hydrophobic properties and reduced oxygen permeability compared to neat PVA films. Furthermore, the integration of MMT nanoclay, even at low concentrations, contributed to the development of nanocomposite films with improved oxygen barrier properties. Consequently, the quadri-layer films demonstrate great potential for food packaging applications.

*Keywords*: Biopolymer; MMT nanoclay; spin-coating; Layer-by-Layer (LbL) technique; multi-layer film; molecular orientation; oxygen permeability

## 1. Introduction

Due to the extensive use of synthetic polymers and their negative environmental impact, along with the increasing need to enhance food preservation, it is crucial to develop biodegradable alternatives for active food packaging [1]. Currently, food packaging heavily relies on synthetic macromolecules derived from petrochemicals, such as polyethylene (PE), polypropylene (PP), polystyrene (PS), polyvinyl chloride (PVC), polyvinylidene

chloride (PVDC), and polyethylene terephthalate (PET) [2, 3, 4, 5]. In addition to providing food protection, plastic films have also been employed to reduce food waste, ensure cost-effective distribution, and benefit from their transparency [6]. In order to address environmental and safety concerns, it is imperative to prioritize the exploration of alternative materials that exhibit biodegradability, recyclability, non-toxicity, and effective antibacterial properties [7]. Intelligent and active packaging plays a vital role in safeguarding against lipid and pigment oxidation, thereby extends the shelf life of food, ensures its safety, and provides valuable information regarding the quality of packaged. Particularly, oxygen barrier plays a pivotal role in food packaging because oxygen is considered as one of the main factors contributing to the deterioration of food products. Numerous food items, such as fats, oils, vitamins, and certain proteins, are exceptionally susceptible to oxidation when exposed to oxygen, leading to the development of undesirable flavors and nutrients' degradation. An oxygen barrier serves to either prevent oxygen from entering, thereby preserving the freshness and overall quality of the food. Furthermore, the presence of oxygen can accelerate the proliferation of some microorganisms, including bacteria [7], which are known culprits behind food spoilage and reduced shelf life. The implementation of an oxygen barrier within the packaging actively inhibits the growth of these spoilage agents, resulting in an extension of the product's shelf life [8]. Oxygen's impact is not limited to flavor and shelf life alone; it also affects the appearance of food products, leading to undesired alterations in the color of certain foods, such as the browning of fruits and vegetables. Through the establishment of an effective oxygen barrier, packaging preserves the original taste and aroma of the product. Achieving an efficient oxygen barrier involves the utilization of diverse packaging materials and technologies and the application of barrier coatings or films. The choice of a specific barrier method hinges on the unique requirements of the food product and its anticipated shelf life.

Over the last two decades, extensive research efforts have been dedicated to enhancing the properties of packaging films to expand their applications. These efforts encompass strategies such as reinforcing with nanomaterials, blending with various biopolymers, incorporating plasticizers, and introducing hydrophobic components [9]. The incorporation of nanoparticles into biopolymer matrices can effectively modify the functional properties of their resulting films [10]. Recent studies have explored the blending of various polysaccharides, including starch [11, 12], chitosan (CS) [13, 14], locust bean gum [15], k-carrageenan, konjac glucomannan, and microcrystalline cellulose [16, 17], with agar to create composite films. Yu et al. [18] employed a casting method to prepare N-(2-hydroxy) propyl-3-trimethylammonium chitosan chloride (HTCC)/PVA composite films and their results demonstrated that the addition of PVA to HTCC significantly enhanced the mechanical properties of the films. Consequently, blending PVA with CS emerges as a promising strategy for developing biodegradable food packaging films with favorable mechanical properties [19]. Also, there has been a notable emphasis on incorporating inorganic fillers with layered structures, such as unaltered clays and clays modified with organic compounds (organoclays), to improve the characteristics of polymeric materials [20, 21]. MMT nanoclay is particularly popular among the various types of layered inorganic clays. It is extensively used in the fabrication of high-performance polymer composites due to its non-toxic nature, excellent strength, abundant availability, and low cost [22, 23]. When layered silicate minerals are combined with polymers, they form a "brick-and-mortar" arrangement that enhances thermal, mechanical, and barrier properties. In a study conducted by Li et al. [24], the non-isothermal crystallization of PVA/MMT composites and their potential decomposition were investigated. The researchers demonstrated that observed changes in molecular structure and crystallization retardation indicate the influence of thermal degradation on the non-isothermal crystallization of PVA/MMT composites.

PVA, a water-soluble polymer, offers the advantage of being able to form nanocomposites from aqueous solutions and produce thin films (ranging from 1 to 200 μm) through water evaporation. These PVA films exhibit flexibility, exceptional visible transparency, good dimensional stability, and remarkable oxygen barrier properties [25]. The impressive oxygen barrier performance can be attributed to the significant intermolecular and intramolecular cohesive energy resulting from the highly polar hydroxyl (-OH) groups present in PVA [26]. It is well known that PVA is a non-toxic polymer with remarkable chemical resistance and physical properties [27, 28]. Nevertheless, it suffers from its low mechanical strength and the above authors explored the incorporation of clay into PVA that leads to a reduction in oxygen permeability at high humidity levels due to the strong interaction between PVA and clay.

Chitosan is a naturally abundant cationic alkaline polysaccharide derived from the deacetylation of chitin, which is primarily found in the exoskeletons of crustaceans and insects, as well as in the cell walls of fungi [29, 30, 31]. Although CS is less prevalent in nature compared to chitin, it is a linear polymer primarily composed of glucosamine units and exhibits polyelectrolyte behavior under acidic pH conditions. It has gained significant recognition in the field of food packaging materials due to its antibacterial properties, renewable nature, biodegradability, and excellent film-forming ability. It possesses the ability to form ionic bonds at low pH values, enabling it to bind with various types of anions. This biodegradable mucoadhesive polysaccharide holds promise

as a biopolymer alternative to plastic food packaging [32]. At the nanoscale level, CS exhibits numerous advantages, including high antibacterial activity, a broad spectrum of activity, and non-toxicity. Consequently, CS is considered as a versatile substance for removing harmful compounds from the environment. Since the demands for food packaging typically include high barrier properties (gas impermeability) and mechanical properties, pure CS films have been found to be inferior to plastic packaging in terms of these properties [33]. As a result, recent research efforts have focused on developing polymer-CS based packaging films to enhance their performance. Various strategies have been explored, such as incorporating additives to improve the properties of CS films and developing functional CS-based food packaging [32, 33]. In particular, the addition of certain additives, including nanoparticles and plant extracts, has been investigated to enhance the properties of CS films [34, 35]. These additives aim to overcome the limitations of pure CS films and improve their barrier properties and mechanical characteristics. Extensive experimentation has been conducted to demonstrate the biomedical potential of chitin, chitosan, and their derivatives [31, 36, 37].

Numerous techniques are currently under investigation for depositing nanocomposite coatings or films, including layer-by-layer (LbL), self-assembly, dip coating, spin-coating, plasma-enhanced or assisted chemical vapor deposition, and more [38]. These techniques hold potential for applications in food packaging. In any of these deposition processes, nanoparticles exhibit a self-organizing behavior, forming a coating that bonds with the surface of the product material. This occurs when the surface is smooth and devoid of pores. However, in the case of porous surfaces, the nanoparticles penetrate the pores, filling them from the inside of the product material. This enables effective coverage and integration of nanoparticles into the porous structure. Based on previous studies conducted by our laboratory [39], the LbL deposition technique has been identified as an effective method for producing thin coatings with improved oxygen barrier properties.

The objective of the current research is to develop active packaging films from biodegradable polymers (PVA and CS) and MMT nanoclay by using the LbL method assisted by the spin coating technique to enhance their oxygen barrier properties by aligning PVA and CS macromolecules and MMT nanoclay parallel to the film's surface during production. For both PVA-MMT and PVA-CS film structures, a combination of PVA/MMT and PVA/CS layers were alternately deposited on a glass substrate during spin coating.

## 2. Materials and methods

### 2.1 Materials

In this work, two polymers were selected: i) Polyvinyl alcohol (PVA) (Mw=146,000 – 186,000 g. mol$^{-1}$, 87–89% hydrolyzed); ii) Chitosan (CS) (190,000<$M_w$<310,000 g. mol$^{-1}$, degree of deacetylation between 75 and 85%). Both polymers were purchased from Sigma Aldrich (Saint Louis, Missouri, USA). Natural sodium montmorillonite (MMT) nanoclay (Cloisite® Na$^+$) density = 2.86 g/cm$^3$) was purchased from BYK USA Inc. (Gonzales, Texas, USA). The substrate used for LbL deposition is a glass slide (3.5cm × 2cm and 1mm in thickness). For the oxygen permeability characterization, larger glass substrates of circular shape (6–7cm in diameter and 1mm in thickness) were used to respect the dimensions of the oxygen permeability equipment of our laboratory. Both substrates were provided by ProAmpac (Terrebonne, QC, Canada).

### 2.2 Film preparation

Various PVA, CS, and MMT solutions with different weight concentrations of CS and MMT were prepared according to our previous study [39]. To create the PVA solution, 7.0 grams of PVA powder were completely dissolved in 100 ml of deionized water under magnetic stirring at 80°C for 2 hours, resulting in a clear white hydrogel. This PVA solution was served as the base matrix for all the films developed in this study. For the CS solutions, different weight concentrations of CS (0.1, 0.4, 0.6 and 1.0 wt.%) were dissolved in 100 ml of a 2% acetic acid solution. The pH of the solution was adjusted to pH 6 by adding acetic acid and 1 mol of sodium hydroxide (NaOH). Similarly, the same procedure was employed for preparing MMT solutions. Four different weight concentrations of MMT (0.5, 1.5, 2.5, and 5 wt.%) were prepared individually in 100 ml of deionized water. The process involved magnetic stirring for 30 minutes, followed by mechanical stirring for 2 hours, and finally, sonication for 15 minutes. Sonication was carried out to prevent any agglomeration of MMT nanoplatelets during the deposition of the charged layer [40]. All MMT solutions were prepared at room temperature, and the pH of the MMT suspensions was maintained at pH 7. To create a primer layer for the films, a polyethylene imine (PEI) solution was utilized. The PEI, obtained from MICA Corporation (Shelton, CT, USA) was applied to the glass slide substrate. The weight concentration of the PEI solution used was 0.6%. To ensure the removal of all

impurities from the glass substrate surface before the deposition of the films, several pre-treatment steps were conducted. The glass slides were initially submerged in a solution consisting of acetone and deionized water for a duration of 15 minutes. Subsequently, they were soaked in deionized water to further cleanse the surfaces.

The fabrication process of the multilayer films involved the utilization of the spin coating technique in a static mode. Here are the three sequential steps that were followed for the fixed glass substrate:

- Step 1: Deposition of the solution: Approximately 1ml of each solution intended for the film coating was deposited onto the substrate. For example, in the case of the PVA-MMT structure, 1ml of PVA and MMT solutions were deposited for each layer coating.
- Step 2: Spin coating and thickness standardization: After deposition, the spin coater was raised to distribute the deposited solutions evenly across the substrate surface, which remained stable due to the vacuum created within the device enclosure. Initially, a rotation speed of 400 rpm was applied for 30 seconds, followed by a rotation at 500 rpm for 1 minute to thin out and standardize the film thickness. The initial low rotation speed was chosen to prevent any overflow of the deposited solution.
- Step 3: Film formation and detachment: Following the evaporation of the residual solvent, the flexible films are then detached from the substrate using a clamp.

The same process was utilized for manufacturing both bi-layer and quadri-layer PVA-MMT and PVA-CS films, encompassing different concentrations of MMT (0.5, 1.5, 2.5, and 5 wt.%) and CS (0.1, 0.4, 0.6 and 1.0 wt.%). **Figure 1** illustrates the equipment used and the sketch of the sequential steps used for the preparation of the spin assisted LbL film structures. For oxygen permeability characterization, thicker films were produced by slight modification of the above procedure. In this case, a 5ml of solution (instead of 1 ml) were deposited for each film layer using a 10ml syringe. The films were then dried at 60°C for 15 minutes, resulting in film thicknesses ranging between 20 and 30 μm.
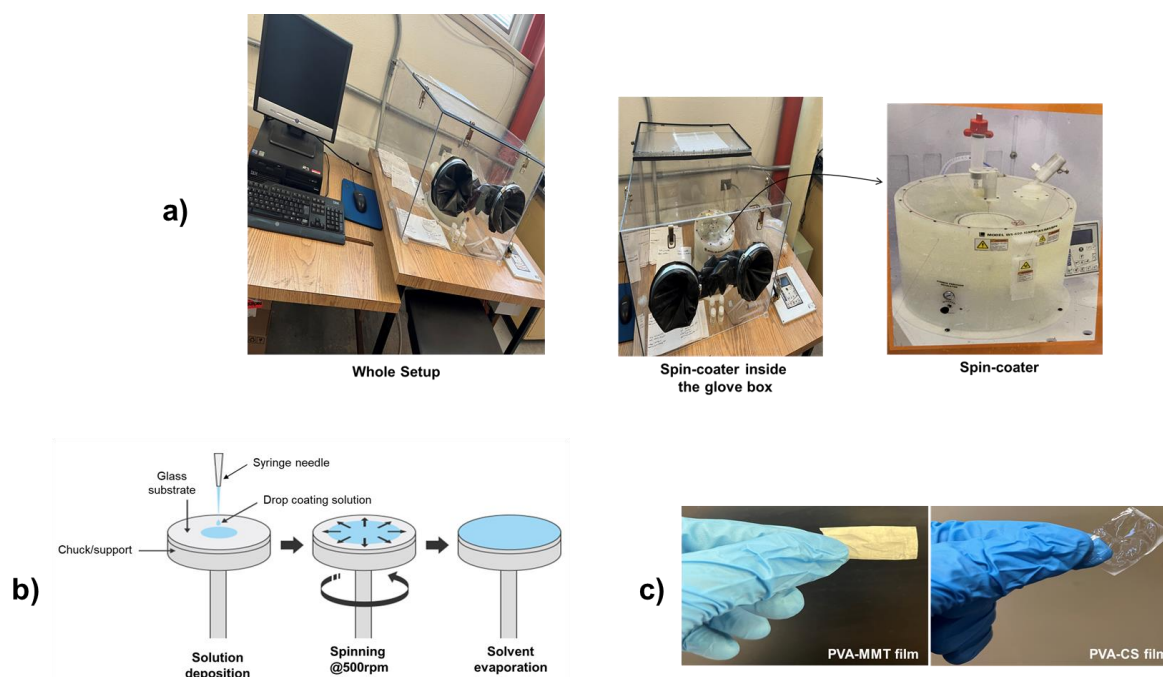


**Figure 1.** Spin-coating setup (a), schematic illustration of films preparation steps (b), and pictures of PVA-MMT & PVA-CS films (c)

## 2.3 Films characterization

### 2.3.1 Two-Dimensional Wide-Angle X-ray Diffraction (2D-WAXD)

In order to assess the orientation and alignment of PVA and CS chains and MMT nanoplatelets within the films, 2D-WAXD analysis was conducted. The latter aids in understanding the dispersion state of charges, allowing for an assessment of the impact of the "Spin-LbL" method on this arrangement. To perform this analysis, 2D-WAXD analysis was carried out on all bi-layer and quadri-layer PVA-MMT and PVA-CS film structures using a Philips X'Pert diffractometer equipped with a general area detector diffraction system operating at 50 kV

and 40 mA in wide-angle mode. The diffraction patterns were obtained by scanning the wide-angle range from 2 to 10 degrees at a speed of 0.02°/s, following the Bragg method. CuKα radiation generated by copper ($\lambda = 1.54056$ Å) was employed as the X-ray source. The 2D diffraction patterns were recorded in transmission mode, while tilting the sample from 0° to 80° relative to the primary X-ray beam. The value of the orientation factor $f$ is determined using the following equation [41]:

$$f = \frac{180° - \psi°}{180°}$$  (1)

where $\psi°$ is the width at half maximum of the azimuthal intensity distribution of the 2D-WAXD peaks.

### 2.3.2 *Fourier-Transform Infrared Spectroscopy (FTIR)*

The application of Fourier-transform infrared (FTIR) spectra enables the assessment and characterization of the interactions occurring among the constituents of composite films, specifically chemical bonds and functional groups of the compounds [42]. To explore these interactions, FTIR measurements were conducted using a JASCO 4600 FT-IR Spectrometer (Japan) equipped with an attenuated total reflectance (ATR) PRO ONE reflection accessory. The spectra were recorded in the 600–4000 cm$^{-1}$ range with a resolution of 4 cm$^{-1}$ and an accumulation of 32 scans in air at room temperature. This approach facilitates the examination of interfacial interactions, chemical bonds, and the emergence of novel functional groups in the PVA-MMT and PVA-CS film structures.

### 2.3.3 *X-ray diffraction Analysis (XRD)*

The amorphous or crystalline nature of the films was assessed using X-ray diffraction (XRD) technique, employing a Siemens / Bruker D5000 X-ray Powder Diffraction (XRD) System. Scans were conducted within a 2θ diffraction angle range of 5°–85°, with a scanning speed of 0.05°/min and a step size of 0.02°. X-ray radiation was generated by a Cu-Kα source (40kW) with a wavelength (λ) of 0.154 nm. This methodology is performed to assess the state of interlayer spacing of the montmorillonite (MMT) and polymer chains on the surface of the composite films, according to the Bragg's law ($\lambda = 2d \sin(\theta)$) where $d$ is distance between the adjacent MMT sheets and $\theta$ is the diffraction angle. The percentage crystallinity $\chi_c(\%)$ was determined using the following equation [43].

$$\chi_c(\%) = \frac{A_c}{A_c + A_a} \cdot 100\%$$  (2)

where $A_c$ and $A_a$ represent the areas of the crystalline and amorphous regions, respectively. Crystallite's size d was calculated using the following Debye-Scherrer equation [44, 45]:

$$d = \frac{K \cdot \lambda}{\beta_{hkl} \cdot \cos\theta}$$  (3)

where $K$ (shape factor) is equal to 0.89, λ is the x-ray wavelength, which is 0.154nm, $\beta_{hkl}$ is the half-width of (hkl) reflection, and $\theta = 2\theta/2$ is the Bragg angle corresponding to (hkl) reflection.

### 2.3.4 *Film thickness measurements*

Film thicknesses were determined using a thickness gauge (7327, Mitutoyo Corporation, Japan) with a precision of 0.001 mm. Measurements were taken at five random positions within the film test area using a 150 mm digital caliper calibrated to 0.01 mm. To obtain an accurate representation, the average of four measurements from different locations on each film was calculated. These thickness measurements were then utilized to evaluate the oxygen permeability properties of each film structure.

### 2.3.5 *Contact Angle (CA) measurement*

Contact angle measurements were conducted at room temperature using an OCA 15+ DataPhysics goniometer from Future Digital Scientific Corp. (Westbury, NY, USA). The CA was determined using the sessile drop method, where a probe liquid of distilled water was employed. An immobile water droplet with a volume of approximately 3 μl was carefully placed on the surface of the film, and the resulting contact angle was measured

in degrees. The measurements were repeated at least five times to ensure accuracy and reliability. The reported CA values represent the mean of the recorded measurements.

### 2.3.6 Oxygen Permeability (OP) measurement

The gas transport properties were evaluated using a variable pressure (constant volume) method [46]. **Figure 2** showcases the experimental setup employed for permeability and selectivity measurements. The measurements were conducted under the following parameters: film test area of 30 cm², test temperature of 25°C, atmospheric pressure (1 atm), and relative humidity of 0%, in accordance with ASTM D-3985-81 guidelines. Prior to each test, the films were mounted within a permeation cell, and the entire apparatus was degassed. The upstream side of the cell was then introduced to the permeant gas, and the pressure on the downstream side was allowed to rise until a constant rate of pressure increase over time was achieved. This constant rate was recorded using a pressure transducer. Each sample was tested three times to ensure accuracy and reliability and only the average value was reported. The permeability coefficient, P [cm$^3$ (STP) cm cm$^{-2}$ s$^{-1}$ (cm Hg)$^{-1}$], was determined using the following equation [47]:

$$P = \frac{22414}{A} \times \frac{V}{RT} \times \frac{l}{\Delta p} \times \frac{dp}{dt} \tag{4}$$

where $A$ is the membrane area (cm$^2$), $l$ is the membrane thickness (cm); $\Delta p$ is the upstream pressure (psi); $V$ is the downstream volume (cm$^3$); $R$ is the universal gas constant (6236.56 cm$^3$ cm Hg mol$^{-1}$ K$^{-1}$); $T$ is the absolute temperature (K); and dp/dt is the permeation rate (psi s$^{-1}$).
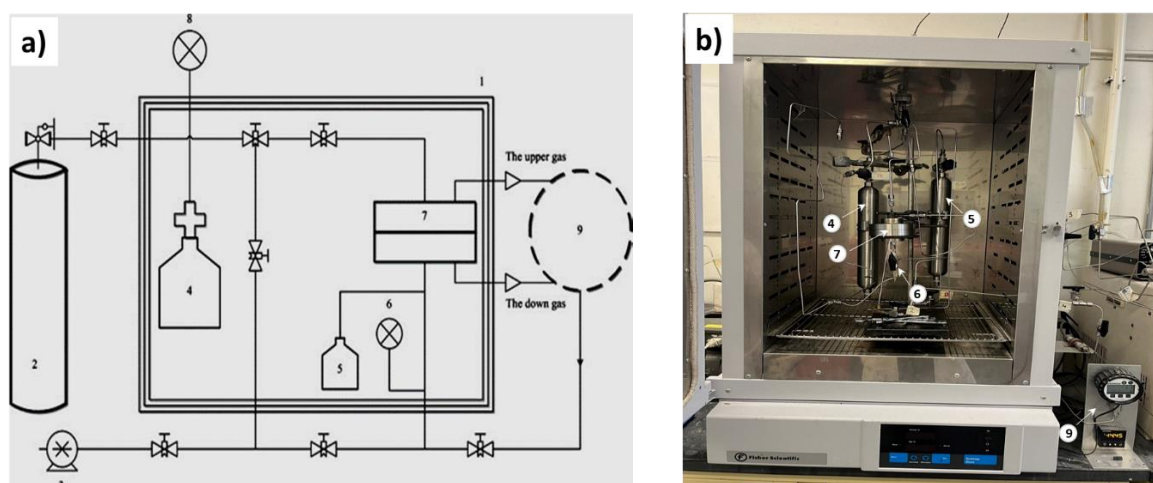


**Figure 2.** Permeability measurement setup: (a) Sketch, and (b) Real picture
**1:** Heated chamber; **2:** supply gas cylinder; **3:** vacuum pump; **4:** the feed reservoir; **5:** the permeate reservoir; **6:** pressure transducer for downstream (15 to 15 psi); **7:** film/membrane cell; **8:** pressure gauge of upstream (0–1000 psi); and **9:** 2-position and 10 ports valve.

### 2.3.7 Differential scanning calorimetry (DSC)

The miscibility of the polymer/polymer layers and/or polymer/nanoparticle layers plays a crucial role in the development of multi-layer films using the LbL technique, as it directly influences the final properties of the films [48]. To explore the miscibility behavior of both bi-layer and quadri-layer film structures, a differential scanning calorimetry (DSC 6000, Perkin-Elmer, Waltham, Massachusetts) was used in this study. The analysis was conducted within a temperature range of 0°C to 260°C, with a linear heating rate of 20°C/min, under a nitrogen flow of 50 mL/min. The characterized samples used for the analysis had a mass of approximately 5mg each.

## 3. Results and Discussion

### 3.1 FTIR characterization

#### 3.1.1 Bi-layer and quadri-layer spin-LbL PVA-MMT films

The interaction at the interface between PVA and MMT layers was studied using FTIR. The corresponding spectra are presented in **Figures 3(a)** and **(b)** for neat PVA films and bi-layer and quadri-layer PVA-MMT films, respectively, with varying MMT weight concentrations (0.5, 1.5, 2.5, and 5 wt.%). The spectrum of neat PVA films exhibits specific peaks indicative of various functional groups. A prominent peak at 3345 cm$^{-1}$ corresponds to the absorption of -OH stretching vibrations, while a vibrational band at 2929.40 cm$^{-1}$ is attributed to the asymmetric stretching vibrations of the aliphatic chain (-CH$_2$). Additionally, a peak at 1725 cm$^{-1}$ is observed, which corresponds to the stretching vibration of the acetate group (-CO-C). In the fingerprint region (<1500 cm$^{-1}$), several peaks were detected, such as those in the range of 1500 to 800 cm$^{-1}$. Notably, the weak intensity peak at 1429.01 cm$^{-1}$ in the PVA spectrum is associated with the -OH bending vibration of the hydroxyl group, while the large bands in the range of 1412-1325 cm$^{-1}$ are attributed to the CH$_2$ groups. Another weak vibration band, appearing as a shoulder at 1250.87 cm$^{-1}$, corresponds to O-H bending vibrations, and the absorption band at 1094.05 cm$^{-1}$ is attributed to C-O stretching of the acetyl groups present in the PVA backbone. The identification of these characteristic groups in PVA aligns with previous studies cited in the literature [49, 50, 51, 52, 53].

For both bilayer and quadri-layer PVA-MMT films, notable characteristics are observed within the frequency range of 3500-3250 cm$^{-1}$. In this frequency range, the dominant vibration modes are attributed to O-H and CH$_2$ stretching. A broad band centered at 3345.50 cm$^{-1}$, attributed to hydroxyl groups in PVA, displayed significant modifications characterized by a broader and more pronounced shape (hump) across all spectra. This suggests an interaction between the hydroxyl groups in PVA and functional groups containing oxygen and GO (graphene oxide) in the MMT layers, indicating the formation of hydrogen bonds. This observation aligns with the findings reported by X. Qi et al., 2014. Furthermore, as the loading of MMT clay increased from 0.5 to 5.0 wt.%, the intensity of several bands in the spectra became larger. Specifically, the bands at 2929.40 cm$^{-1}$ (CH$_2$ stretching), 1725.84 cm$^{-1}$ (stretching vibration of the acetate group), 1250.87 cm$^{-1}$ (O-H bending vibration), 1094.05 cm$^{-1}$ (C-O stretching of acetyl groups), and 840.46 cm$^{-1}$ exhibited increased intensity in all bi-layer and quadri-layer PVA-MMT films.
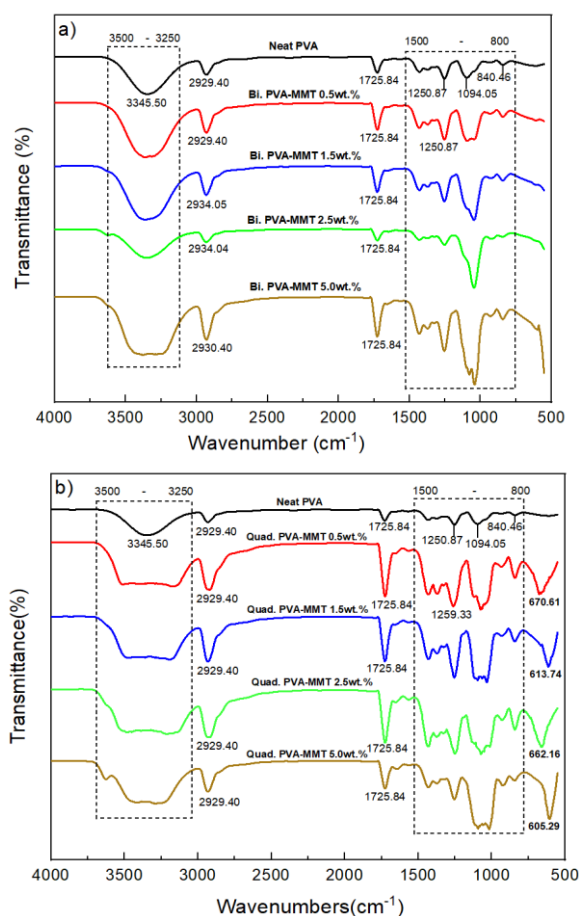


**Figure 3.** FTIR spectra of spin-LbL PVA-MMT films: (a) bi-layer structure, and (b) quadri-layer structure

### 3.1.2 Bi-layer and quadri-layer spin-LbL PVA-CS films

**Figures 4(a)** and **(b)** display the FTIR spectra of neat PVA, neat CS, as well as bi-layer and quadri-layer PVA-CS films. As shown, the spectra of both bilayer and quadri-layer PVA-CS films exhibit similarities, primarily due to the consistent interactions occurring between the PVA and CS layers. The spectra of neat PVA and PVA-CS films exhibit the stretching vibration peak of the O-H bond at 3445.5 cm$^{-1}$ [54]. Within the frequency range of 3500-3250 cm$^{-1}$, this peak becomes more intense and broader in both bi-layer and quadri-layer PVA-CS films compared to that of neat PVA film. The Figure also shows that with an increase in CS weight concentration in both bi-layer and quadri-layer films, the intensity and width of the bands at 2929.40, 1725.84, 1250.87, 1094.05, and 840.46 cm$^{-1}$ increase. This phenomenon may be attributed to the overlapping of peaks from PVA and CS spectra, facilitated by the formation of new hydrogen bonds [55]. Consequently, there are robust interactions between these functional groups and the -OH groups of PVA, leading to a noticeable shift towards lower wavenumbers. Interestingly, for both bi-layer and quadri-layer films, we observe the emergence of a new peak around 1570.06-1582.12 cm$^{-1}$, which is absent in neat PVA spectrum. This additional peak is likely attributed to the bending vibration of the -NH$_2$ group, possibly overlapping with the vibration of amide II. Furthermore, the peak at 1430.18 cm$^{-1}$ in the PVA spectrum experiences a shift to 1420.72 cm$^{-1}$ in the spectra of the bi-layer and quadri-layer PVA-CS films. This shift suggests interactions between the -OH and -NH$_2$ groups, potentially involving hydrogen bonding, without any evident formation of covalent bonds between PVA and CS [55].

In general, when the layers of PVA-CS films tend to mix, either through physical or chemical interactions, differences in the spectra bands can be observed. This phenomenon is evident all PVA-CS spectra, indicating a possibility of semi-miscibility between the PVA and CS layers.
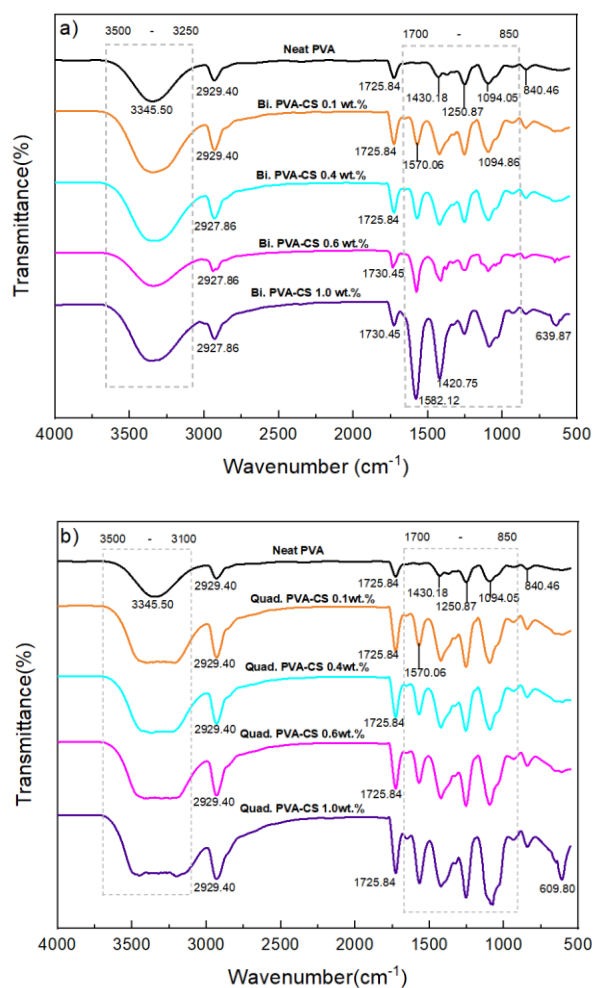


**Figure 4.** FTIR spectra of spin-LbL PVA-CS films: (a) bi-layer structure, and (b) quadri-layer structure

## 3.2 DSC characterization

### 3.2.1 Bi-layer and quadri-layer spin-LbL PVA-MMT films

In this study, the crystallization behavior of bi-layer and quadri-layer PVA-MMT films with varying weight concentration of MMT (0.5, 1.5, 2.5, and 5 wt.%) was investigated using differential scanning calorimetry (DSC) under $N_2$ atmosphere, with a heating rate of 20°C/min, in the temperature range of 0°C to 260°C. The corresponding thermograms are presented in **Figures 5(a)** and **(b)**. The DSC thermogram of pure PVA exhibits an initial endothermic peak around 63.5°C, corresponding to its glass transition temperature ($T_g$). Another endothermic peak is observed around 194°C, corresponding to its melting temperature (Tm). These values are consistent with those reported in previous literature [42, 56]. The thermograms of the bi-layer PVA-MMT films (**Figure 5(a)**) reveal an increase in the $T_g$ values from 58.8°C to 65.33°C as the MMT weight concentration increases from 0.5 to 5.0 wt.%. This phenomenon can be attributed to the presence of MMT nanoplatelets dispersed between the polymer chains, which restrict their segmental movement [57, 58]. However, the presence of MMT fillers does not appear to exert any influence on the melting temperature values of the various bi-layer films. On the other hand, the thermograms of the quadri-layer PVA-MMT composite films shown in **Figure 5(b)** exhibits robust and relatively broad endothermic peaks at 57.72°C, 61.05°C, 58.49°C, and 64.13°C, corresponding the $T_g$ of PVA-MMT films with 0.5, 1.5, 2.5, and 5 wt.% MMT, respectively. Moreover, the thermograms reveal sharper and more intense melting peaks at around 193.45°C attributed to the increased number of layers from 2 to 4, mainly for 1.5 and 2.5 wt.% MMT.
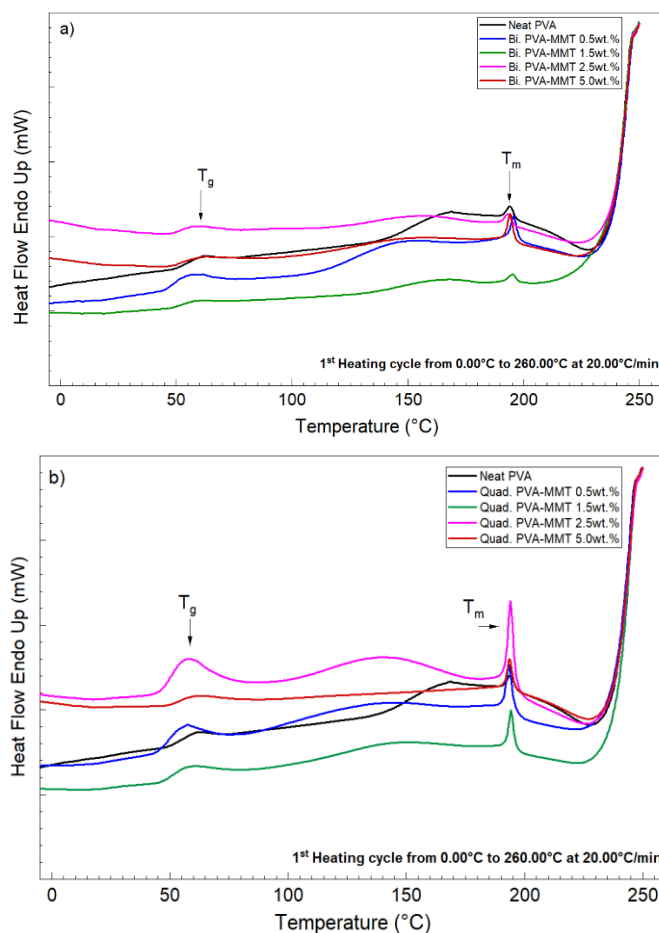


**Figure 5.** DSC curves of spin-LbL PVA-MMT films: (a) bi-layer structure, and (b) quadri-layer structure

### 3.2.2 Bi-layer and quadri-layer spin-LbL PVA-CS films

DSC characterization of PVA-CS films with different CS weight concentrations (0.1, 0.4, 0.6, and 1.0 wt.%) was performed under the same conditions as PVA-MMT films. **Figures 6(a)** and **(b)** present the corresponding thermograms for both bilayer and quadri-layer films. As shown, the bi-layer PVA-CS films exhibit a behavior

similar to that of the neat PVA film. The first endothermic peaks, characterized by relatively broad profiles and low intensities, appear around 68.21°C for the bi-layer films with 0.1 and 0.4 wt.% CS. For 0.6 and 1.0 wt.% CS, the endothermic peaks are observed at approximately 71.05°C and 74.12°C, respectively. These peaks are slightly shifted towards higher temperatures compared to the endothermic peak of the monolayer PVA film, indicating the presence of $T_g$ transition in the bilayer films. On the other hand, the DSC thermograms of the quadri-layer films with 0.1, 0.4, 0.6, and 1.0 wt.% CS show broad endothermic peaks at about 82.09°C, 75.01°C, 68.05°C, and 67.25°C, respectively. These endotherms occur at higher temperatures compared to both neat PVA film and the bi-layer PVA-CS films. They can be due to the evaporation of water molecules and residual solvents used during the film preparation [59]. The second endothermic peaks manifest as broad peaks or bumps, particularly in quadri-layer films with 0.6 and 1.0 wt.% CS. For films with 0.1 and 0.4 wt.% CS, these peaks are observed at temperatures around 198.14°C and 198.88°C, respectively, corresponding to their respective melting temperatures ($T_m$). For films with 0.6 and 1.0 wt.% CS, they exhibit a shift towards lower temperatures, specifically to 184.28°C and 184.78°C, respectively.
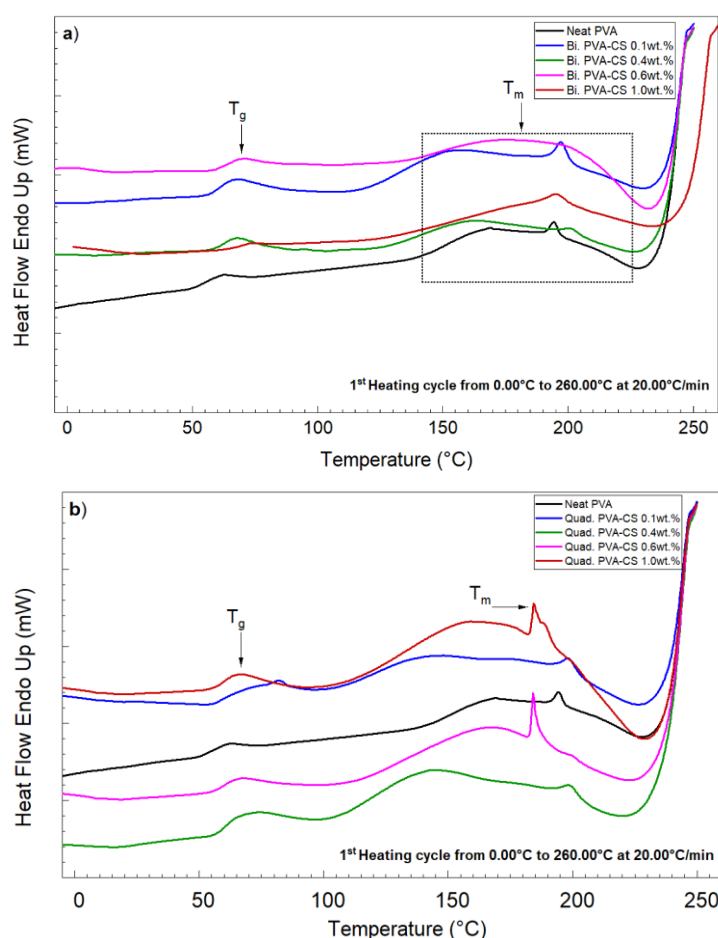


**Figure 6.** DSC curves of spin-LbL PVA-CS films: (a) bi-layer structure, and (b) quadri-layer structure

## 3.3 2D-WAXD characterization

In order to capture the complete range of orientation space, 2D-WAXD patterns were obtained using an image plate equipped with a 2 mm aperture. The measurements were conducted in reflection mode, covering both the polar angle ($\alpha = 0 - 90°$) and azimuth ($\beta = 0 - 360°$). By employing the Bragg equation, the interlayer spacings (d) between MMT nanosheets were calculated. The 2D-WAXD images were acquired with an X-ray beam directed perpendicular to the plane of the film surface, allowing for the collection of diffraction data from the polar figures.

### 3.3.1 Bi-layer and quadri-layer spin-LbL PVA-MMT films

**Figures 7(a)** and **(b)** display the diffractogram spectra of neat PVA and PVA-MMT films containing different weight concentrations of MMT, ranging from 0.5 to 5.0 wt.%. Upon observation, the 2D-WAXD arc patterns (located to the right of the spectra) exhibit isotropic Debye-Scherrer rings for both neat PVA and both bi-layer and quadri-layer PVA-MMT films. The intensity of the diffractograms was normalized using the peak intensity at $2\theta = 19.5°$, which corresponds to the mixture of the (101) and (200) planes. This peak intensity was obtained by extracting the intensity trace along the equatorial axis. The normalization process was carried out to account for the random orientation of crystal unit cells of PVA perpendicular to the film surface as demonstrated in literature [41, 60].

In the spectrum of neat PVA film, a weak peak is observed at $2\theta = 40.8°$, which corresponds to the reflection of the (111) plane of the monoclinic unit cell. This peak is attributed to the semi-crystalline nature of PVA [61]. On the other hand, for PVA-MMT bi-layer and quadri-layer films, this peak becomes more pronounced with increasing the weight concentration of MMT (from 0.5 to 5.0 wt.%) and the number of layers (from 2 to 4 layers). Additionally, the equatorial arc becomes progressively more intense and narrower, aligning with the trend of narrowing observed in the azimuth peak at $2\theta = 19.5°$. These observations indicate anisotropy and an increase in the orientation factor, $f$. The increase in $f$ suggests a gradual enhancement in the orientation of MMT nanoplatelets relative to the film surface. The orientation factor of the MMT platelets relative to the film surface was determined for the quadri-layer PVA- MMT film with 5.0 wt.% MMT. It ranges from 1 to -1/2, where a value of 1 indicates a parallel orientation to the film surface and -1/2 suggests a vertical orientation of the MMT platelets. The calculated average value of $f$ (001) is approximately 0.94, indicating that both the MMT nanoplatelets and PVA polymer chains are predominantly oriented parallel to the surface of the quadri-layer film.
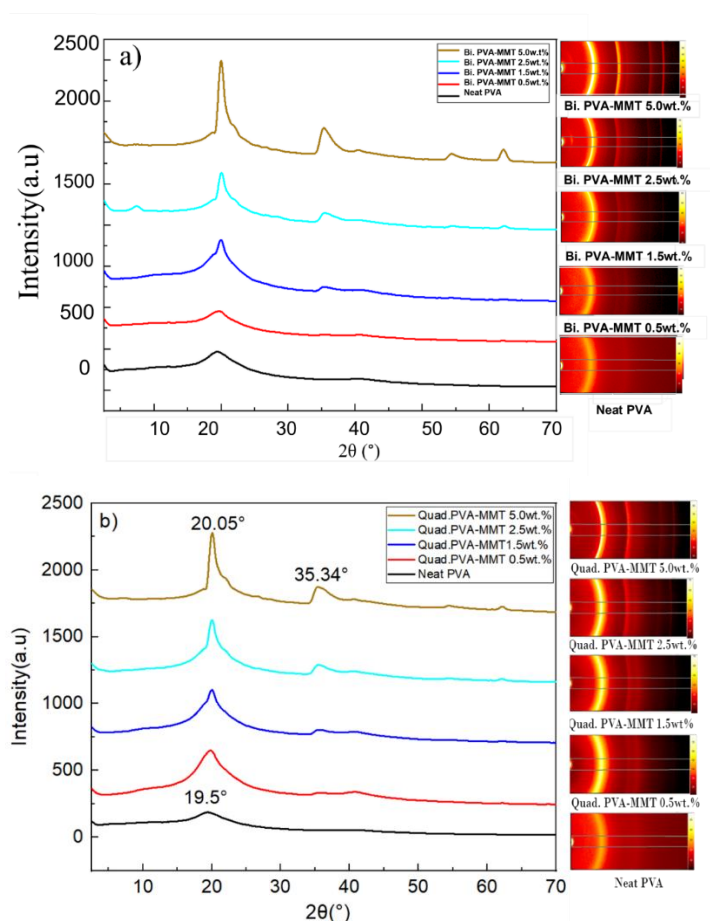


**Figure 7.** 2D-WAXD diffractograms of spin-LbL PVA-MMT films: (a) bi-layer structure, and (b) quadri-layer structure

### 3.3.2 Bi-layer and quadri-layer spin-LbL PAV-CS films

**Figures 8(a)** and **(b)** present the diffractogram spectra of neat PVA and Spin-LbL PVA-CS films at different weight concentrations of CS (0.1, 0.4, 0.6 and 1.0 wt.%) and their corresponding 2D-WAXD arc patterns (located to the right of the spectra). As shown, the 2D-WAXD pattern of the PVA-CS bi-layer film containing 0.1wt.% of CS exhibited a broad and less intense diffraction ring. This anisotropic pattern can be normalized by comparing

it to the diffraction peaks located near the reflections of the (200) and (220) planes of the CS crystals, as well as the $2\theta = 19.5°$ reflection of the (101) plane of PVA. As the CS concentration increased from 0.4 to 1.0 wt.% and the number of layers in the PVA-CS films increased, the equatorial 2D-WAXD patterns demonstrated an initial widening and intensification. This suggests an increased anisotropy and orientation factor (*f*), consequently enhancing the preferential alignment of CS macromolecular chains parallel to the film surface. A newly observed diffraction peak emerged at $2\theta = 8.9°$ in the spectrograms of both bi-layer and quadri-layer PVA-CS films, which is attributed to the (020) reflection of CS crystalline structure [62, 63]. Furthermore, the reflections corresponding to the (200) and (220) planes exhibited a slight widening and a shift of approximately 0.3° towards lower diffraction angles. This suggests an increased spacing between CS crystals due to the reorganization of hydrogen bonds among the CS chains. Moreover, the intensities of the equatorial pattern in the 2D-WAXD models gradually intensified both in the out-of-plane and in-plane directions. The orientation factor (*f*) increased from 0.770 to 0.803 in the out-of-plane direction. These results indicate an improvement in the alignment and orientation of the macromolecular chains, likely due to the centrifugal forces associated with the spin coating method. During the fabrication process of the multilayer films using the spin coating technique, the majority of CS chains in both amorphous and crystalline regions align and orient themselves along centrifugal direction due to the rotation of the substrate. This leads to the formation of a highly oriented structure in the presence of water molecules [64, 65, 66]. During solvent evaporation under external force, the hydrogen bonding interactions between neighboring CS and PVA chains increase significantly leading to the alignment and orientation of PVA and CS macromolecular chains and consequently to densely stratified structures. For both bi-layer and quadri-layer PVA-CS films, a strong diffraction is observed for the (020) reflection in the in-plane direction, indicating that the CS unit meshes are nearly parallel to the film's surface. Consequently, this alignment should enhance the barrier properties of PVA-CS multi-layer films, which will be demonstrated later in section 3.6.
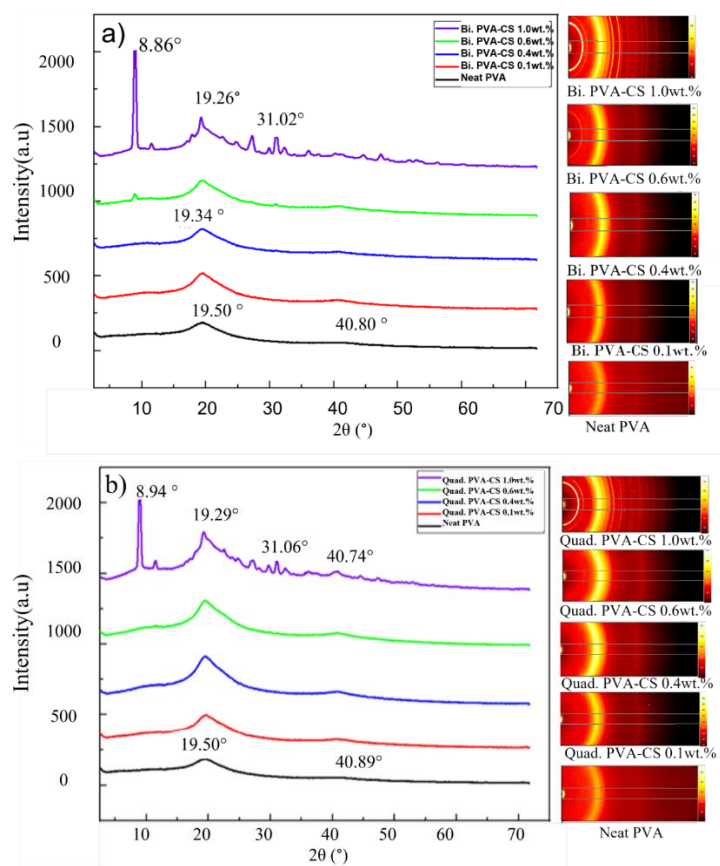


**Figure 8.** 2D-WAXD diffractograms of spin-LbL PVA-MMT films: (a) bi-layer structure, and (b) quadri-layer structure

## 3.4 X-ray diffraction (XRD) characterization

### 3.4.1 Quadri-layer spin-LbL PVA-MMT films

The XRD of the neat PVA, MMT, and quadri-layer PVA-MMT films are shown in **Figure 9(a)** and their corresponding crystallographic parameters are reported in **Table 1**. In the range of 2θ between 5°-10°, the neat PVA spectrum does not show any diffraction peak compared to MMT, which shows a peak at $2\theta = 8.22°$ attributed to the crystallographic plane (001) [67, 68]. According to the Bragg's law ($n\lambda = 2d\sin\theta$), this peak allows to determine the d-spacing ($d_{001}$) between the ordered layers of the (001) plane of MMT in the PVA-MMT film structure ($d_{001}$=1.050 nm) [69, 70]. For the quadri-layer PVA-MMT film with 5.0 wt.% MMT, this peak shifted slightly to smaller angles ($2\theta = 8.04°$) corresponding to an interlayer spacing ($d_{001}$) of 1.109 nm. This suggests the presence of exfoliated layers of MMT dispersed in the PVA matrix [71]. In general, the intercalation of PVA chains between the MMT clay interlayers increases the interlayer spacing, leading to a displacement of the diffraction peak towards lower angle values [72, 69, 73, 74, 75]. When PVA is combined with MMT in quadri-layer film structure, the main peak of neat PVA at $2\theta = 19.45°$ is slightly shifted to higher characteristic angles ($2\theta = 19.86°$ for 0.5wt.% MMT and $2\theta = 19.70°$ for 5.0wt.% MMT), which corresponds to a decrease of interlayer spacing from 0.454 nm to 0.443 nm and 0.446 nm, respectively. This suggests that the MMT platelets are exfoliated within the PVA matrix [76]. With increasing MMT weight concentration from 0.5 wt.% to 5 wt.%, **Figure 9(a)** shows a decrease in the intensity of the main peak at $2\theta = 19.86°$, indicating a decrease in PVA crystallinity, $\chi_c$, from 91% to 88% (**Table 1**). However, the spectrum reveals two sharp and intense peaks at $2\theta = 8.04°$ and $2\theta = 28.66°$. These strong reflections indicate that the MMT nanoplatelets exhibit preferential growth along the PVA matrix plane. Additionally, the diffraction peaks associated with MMT clay at $2\theta = 18.14°$, 20.05°, 36.67°, 46.83°, and 67.84° are completely absent in the diffractogram, which is an indication of a good dispersion and intercalation of MMT platelets, leading to the formation of intercalated-exfoliated nanostructures [77].

### 3.4.2 *Quadri-layer spin-LbL PVA-CS films*

The XRD spectra of neat PVA and quadri-layer PVA-CS films (with CS concentrations of 0.1 and 1.0 wt.%) are presented in **Figure 9(b)**. As mentioned above in section 3.4.1, the spectrum of neat PVA film does not exhibit any diffraction peak in the 2θ range of 2 to 10°. However, it shows a prominent main diffraction peak at $2\theta = 19.45°$, corresponding to an interlayer spacing of d = 0.454nm for the (101) plane [74, 75]. Furthermore, the spectrum of the quadri-layer PVA-CS film with 0.1 wt.% CS closely resembles that of the neat PVA film. This similarity suggests that the PVA layer retains its independent semi-crystalline structure, with only minimal influence from the presence of CS at low weight concentration (0.1 wt.%). On the other hand, the intensity of the main peak is significantly increased compared to the neat PVA, indicating that the crystallinity of PVA is enhanced by the addition of CS. Also, the spectrum shows a slight shift of the main peak towards higher 2θ angles ($2\theta = 19.53°$), possibly due to the formation of intermolecular and intramolecular hydrogen bonds between the -OH groups of PVA and the $-NH_2$ groups of CS. These hydrogen bonds suggest excellent compatibility between the PVA matrix and CS, allowing for increased molecular movement and a higher degree of crystallization of the film. However, at higher CS weight concentration (1.0 wt.%), the main peak intensity of the PVA-CS film slightly decreases compared to the 0.1 wt.% CS film. This decrease is attributed to the enhanced interaction between CS ($-NH_2$ or -OH groups) and PVA (-OH group), leading to the formation of more intra and intermolecular hydrogen bonds. This enhanced interaction limits the movement of CS and PVA chains and results in a strong reduction in the degree of crystallinity in the PVA-CS (1wt.%) film ($\chi_c$= 55%) (**Table 1**).
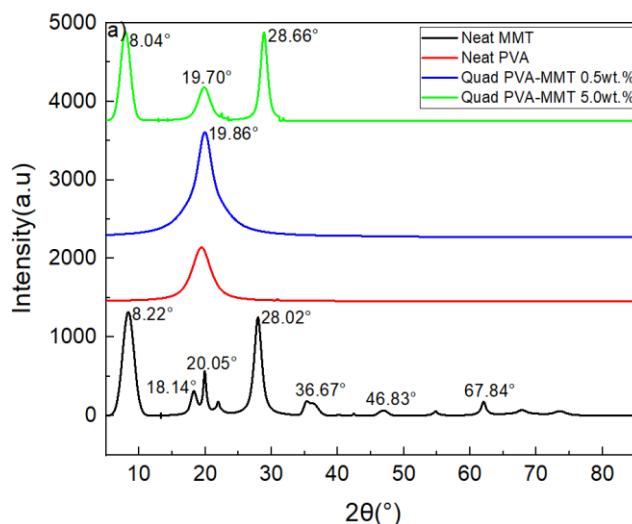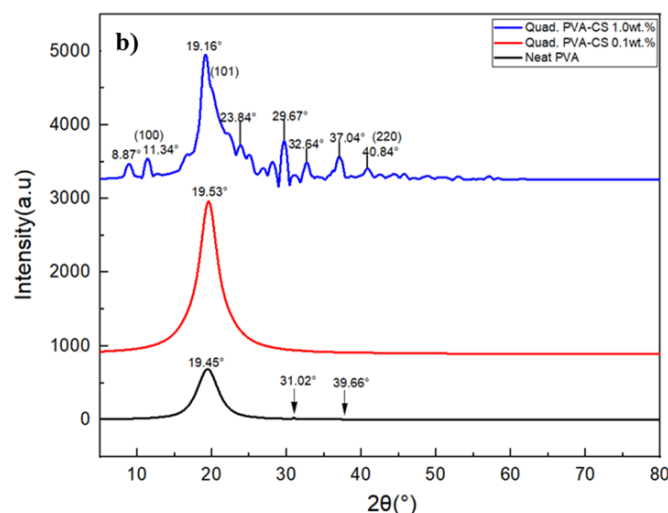
**Figure 9.** XRD patterns of neat MMT, PVA and quadri-layer film structures: (a) PVA-MMT structure, and (b) PVA-CS structure

**Table 1.** Crystallographic parameters of PVA and quadri-layer PVA-MMT and PVA-CS films with different MMT and CS weight concentrations

| Parameters → <br> Films structure ↓ | K(-) | λ (Å) | 2 θ (°) | β (°) | $\chi_c$(%) <br> Equ. (2) | d (nm) <br> Equ. (3) |
|---|---|---|---|---|---|---|
| PVA | 0.89 | 1.5406 | 19.45 | 3.90 | 85 | 20.63 |
| MMT | 0.89 | 1.5406 | 15.95 | 1.51 | 78 | 65.02 |
| Quad.PVA-0.5wt.% MMT | 0.89 | 1.5406 | 19.86 | 4.85 | 91 | 16.26 |
| Quad. PVA-5.0wt.% MMT | 0.89 | 1.5406 | 19.70 | 4.58 | 88 | 47.58 |
| Quad. PVA-CS (0.1wt.%) | 0.89 | 1.5406 | 19.53 | 4.34 | 93 | 18.42 |
| Quad. PVA-CS (1.0 wt.%) | 0.89 | 1.5406 | 19.16 | 4.31 | 55 | 18.58 |

## 3.5 Hydrophobicity/hydrophilicity characterization

The contact angle (CA) with liquids, such as water, is an essential parameter for characterizing the wettability of packaging films. The CA of water droplets varies based on the density of free hydroxyl groups present on the surface of the film. These hydroxyl groups can form hydrogen bonds with water. A lower CA value indicates a more hydrophilic surface of the film. Generally, a CA greater than 90° is a characteristic of hydrophobic surfaces, while that less than 90° is a characteristic of hydrophilic surfaces [78].

The CA for both bi-layer and quadri-layer PVA-MMT and PVA-CS films was measured at room temperature using the sessile drop method and distilled water was used as the probe liquid. The images of the drop were taken about 5 seconds after drop deposit on the surface of the film. The corresponding results are presented in **Figures 10 (a)** and **(b)** and correspond to the average of 3 readings taken at different locations on the surface of the sample. For the four MMT weight concentrations studied (0.5, 1.5, 2.5 or 5 wt.%), **Figure 10(a)** shows that both bi-layer and quadri-layer PVA-MMT films have higher CA values compared to the neat PVA film, which exhibited a hydrophile surface (CA= 54°) due to the abundance of hydroxyl groups on its surface. Additionally, the CA increased from 54° for neat PVA to 83.3° with 2.5 wt.% of MMT for bilayer films, and to 173.2° for 2.5 wt.% MMT in quadri-layered films. However, with higher MMT concentration, the water contact angles decreased for all film surfaces, which could be due to MMT agglomeration. The Figure also shows that, for the same MMT weight concentration, the quadri-layer films displayed higher CA, i.e., greater hydrophobicity than the bilayer films. The increase in hydrophobicity is primarily attributed to the decrease in the number of available hydroxyl groups on the surfaces of both bi-layer and quadri-layer PVA-MMT films. This reduction results from a combination of chemical interactions and structural modifications occurring within the films. The surface hydroxyl groups of MMT nanoclay form strong hydrogen bonding interactions with the hydroxyl groups present on the PVA polymer chains. Consequently, these interactions lead to a decrease in the quantity of free hydroxyl groups available on the surface of PVA-MMT film. The enhanced hydrophobicity observed in quadri-layer films, as opposed to bilayer films, can be attributed to various factors related to the film's composition and structure, as

well as the interaction between the PVA macromolecules and MMT nanoclay. In quadri-layer films, the presence of additional layers (comprising one layer of MMT and one layer of PVA) results in an increased number of interfaces between the MMT nanoclay and the PVA matrix. This heightened interface fosters greater intermolecular interactions, predominantly in the form of hydrogen bonds, between the clay particles and the PVA polymer chains. These interactions, in turn, limit the availability of hydrophilic functional groups on both the PVA and clay surfaces, consequently rendering the film more hydrophobic. Furthermore, the incorporation of an additional layer of MMT nanoclay and PVA can induce alterations in the overall structure of the film. This modification leads to a denser and more tightly packed film, reducing the exposure of hydrophilic groups to the film's surface. Consequently, the film becomes less susceptible to water absorption and exhibits heightened hydrophobic characteristics.

For PVA-CS films (**Figure 10(b)**), both bi-layer and quadri-layer structures show a CA higher than the neat PVA film, as in the case of PVA-MMT films. In both film structures, the CA increases with increasing CS weight concentration up to 0.6 wt.% CS for the bi-layer film (CA= 80.5°) and 0.4 wt.% CS for the quadri-layer film (CA= 115.3°). The highest contact angle of 115.3° for the quadri-layer structure shows its hydrophobic behavior resulting from the increase in the interaction between PVA and CS, which in turn reduces the number of hydroxyl groups exposed on the surface [79].
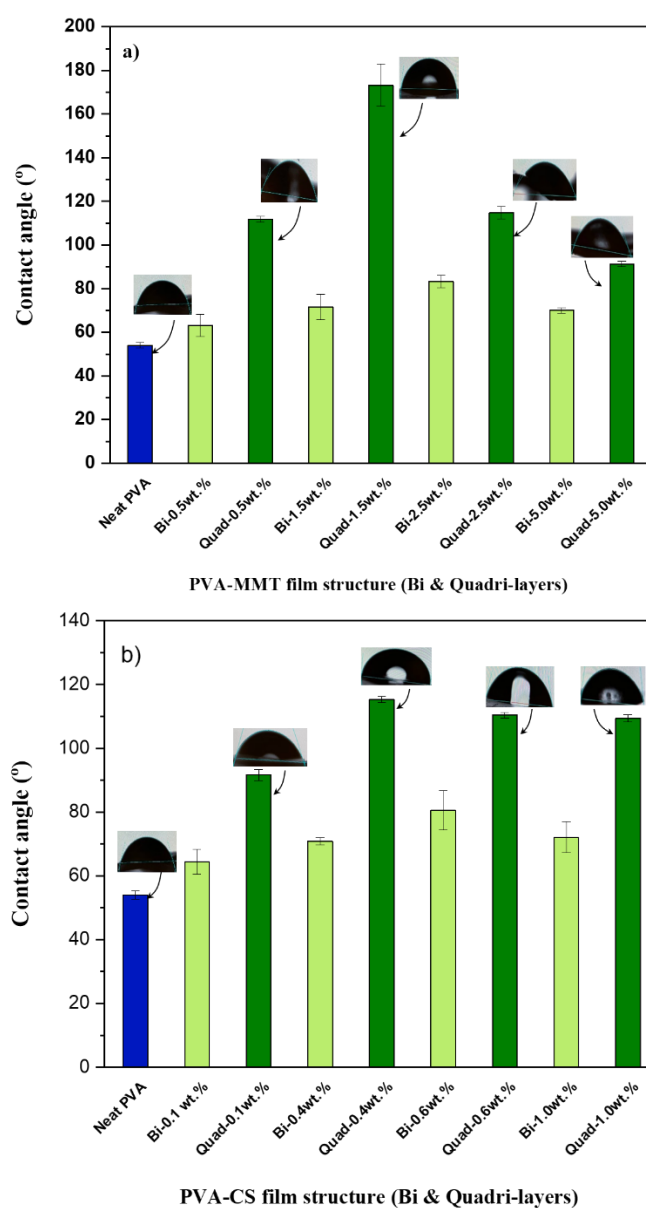


**Figure 10.** Water contact angle for neat PVA and bi-layer and quadri-layer film structures at various MMT and CS weight concentrations: (a) PVA-MMT films, and (b) PVA-CS films

## 3.6 Oxygen permeability characterization

The presence of an oxygen barrier is a crucial aspect of food packaging as it plays a significant role in extending the shelf life of food. To achieve this, it is essential to maintain a packaging environment with a low oxygen content [42]. The measurement of oxygen permeability (OP) serves as an important indicator to assess the ability of transportation for oxygen.

### 3.6.1 Bi-layer and quadri-layer spin-LbL PVA-MMT films

An understanding of the orientation of MMT nanoclay and its interactions within the PVA matrix allow for a much deeper interpretation of oxygen permeability (OP), which is presented in **Figure 11(a)**. PVA is known for its significant interaction with MMT nanoclay, particularly for thin coatings [79, 80]. Compared to the neat PVA film, which has an OP of $6.98 \times 10^{-5}$ Barrer, both bi-layer and quadri-layer structures possess lower OP, which decreases with increasing MMT weight concentration up to 2.5 wt.%. However, an increase in OP is observed for MMT concentration of 5 wt.%, which could be explained by MMT agglomeration. A more interesting result is that, for the same MMT concentration, the OP was much lower for the quadri-layer PVA-MMT film structure. For MMT concentration of 2.5 wt.%, the lowest OP value of $1.42 \times 10^{-8}$ Barrer was obtained for the quadri-layer structure compared to $1.56 \times 10^{-5}$ Barrer for the bilayer structure. These findings align with the outcomes documented in literature [81]. Additionally, by adopting a similar LbL approach, we already achieved an OP of $0.2$ cc·µm/(m$^2$·day·atm) by employing 15 alternating layers of PVA and 15 layers of MMT using the scrape coating method [39]. The decrease in OP clearly indicates that the inclusion of MMT nanoclay, dispersed on the surface of the PVA layers, establishes a convoluted pathway for oxygen molecules, resulting in a reduced OP.

### 3.6.2 Bi-layer and quadri-layer spin-LbL PVA-CS films

CS is known for its effective gas barrier properties due to its molecular structure. Comparing bi-layer to quadri-layer film structures, the latter exhibits improved intermolecular interaction because of the presence of more CS layers. The CS layers facilitate the formation of more hydrogen bonds within the film, resulting in lower OP, i.e., enhanced oxygen barrier properties, as shown in **Figure 11(b)**. As in the case of PVA-MMT films, both bi-layer and quadri-layer PVA-CS structures possess much lower OP compared to neat PVA film and the OP values are lower than in the PVA-MMT films even at lower CS weight concentrations. Also, for the same CS weight concentration, the OP was much lower for the quadri-layer film structure.
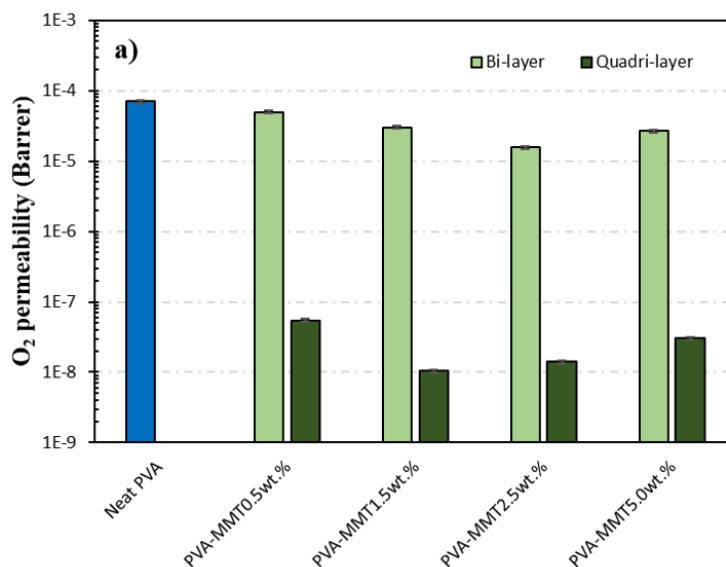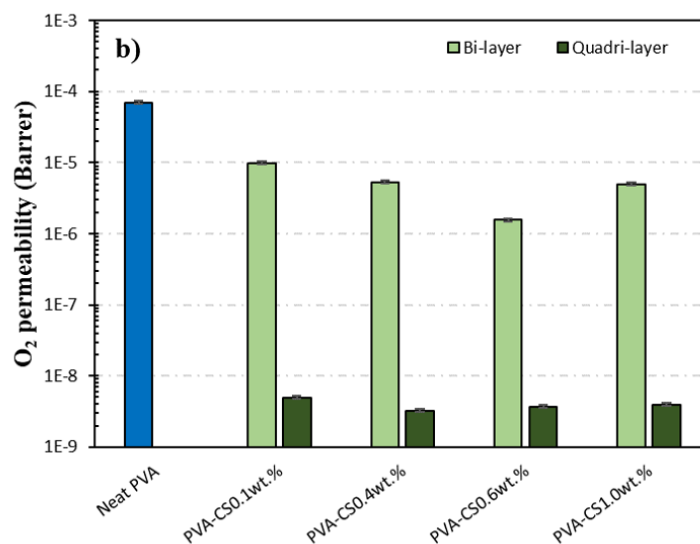
**Figure 11.** Oxygen permeability for neat PVA and bi-layer and quadri-layer film structures at various MMT and CS weight concentrations: (a) PVA-MMT films; and (b) PVA-CS films. Nb: measurement uncertainty is around 5%, so error bars are very narrow on log scale

In the case of both PVA/MMT and PVA/CS bilayer as well as quadri-layer films, the FTIR characterization detailed in section 3.1 illuminates a noteworthy transformation in the hydroxyl (-OH) groups within PVA. These transformations stem from their interaction with the functional groups containing OH and $O_2$ within the MMT layers and $NH_2$ or OH groups within the CS layers. Such interactions unequivocally signify the formation of hydrogen bonds, which, in turn, contribute significantly to the enhancement of oxygen barrier properties. This assertion is further substantiated by the high orientation factor derived from the 2D-WAXD characterization (section 3.3), denoting a prominent alignment of MMT nanoplatelets and PVA or CS polymer chains parallel to the film's surface—whether bilayer or quadri-layer. This alignment fosters increased tortuosity, subsequently improving the film's oxygen barrier capabilities. Moreover, the XRD characterization (section 3.4) of PVA/CS bilayer and quadri-layer films corroborates the augmented interaction between CS (-$NH_2$ or -OH groups) and PVA (-OH group). This intensified interaction manifests in the formation of a greater number of intra and intermolecular hydrogen bonds. Notably, a similar heightened interaction is observed in PVA/MMT bilayer and quadri-layer films, wherein intercalated-exfoliated PVA/MMT nanostructures were observed.

## 4. Conclusions

In this paper, we successfully developed bi-layer and quadri-layer PVA-MMT and PVA-CS film structures using the layer-by-layer technique combined with spin coating. We focused on analyzing the molecular chain orientation of both PVA and CS and the dispersion and orientation of MMT nanoplatelets within their corresponding multi-layer film structures.

For both bi-layer and quadri-layer spin-LbL PVA-MMT structures, the inclusion of MMT nanoplatelets led to a moderate increase in film crystallinity. In comparison, the spin-LbL PVA-CS films exhibited a crystallinity similar to that of the neat PVA film but were more transparent than the PVA-MMT films. These findings indicate that the interaction between PVA and MMT nanoplatelets influences MMT dispersion and orientation, and consequently the permeability of their corresponding bi-layer and quadri-layer PVA-MMT film structures. The orientation factor $f_{(001)}$ yielded an average value of approximately 0.94, indicating that both the MMT nanoplatelets and the PVA chains exhibited parallel orientation with the film surface.

For both bi-layer and quadri-layer spin-LbL PVA-CS films, both structures exhibited prominent X-ray diffraction signals corresponding to the (020) reflection aligned with the CS unit cell plane. This observation suggests that these unit cells are nearly parallel to the film surface. Such a distribution pattern enhances the gas and moisture barrier properties of the PVA-CS films. Additionally, contact angle measurements performed on the quadri-layer PVA-CS structures revealed their hydrophobic nature, as indicated by values exceeding 90°. This behavior can be attributed to the interaction between the functional groups present in the different film layers.

Hence, the combination of LbL technique with the spin coating has demonstrated its efficacy in reducing film oxygen permeability. This reduction becomes more pronounced as the weight concentration of MMT and CS

increases. Furthermore, the quadri-layer film structures exhibited superior oxygen impermeability compared to the bi-layer structures, validating the findings of the orientation analysis conducted through 2D-WAXD. Therefore, the LbL technique combined with spin coating proved to be highly advantageous for the production of films with enhanced oxygen barrier properties with enhanced functional properties. These outcomes hold promising implications for active food packaging applications.

## Acknowledgments

## Conflict of interest

There is no conflict of interest for this study.

## References

[1] J. C. A. Chapal, Biodegradable materials based on poly(vinyl alcohol) (PVA) and poly (lactic acid) (PLA) with antioxidant and antimicrobial activity for food packaging applications, Universitat Politecnica de Valencia, (2021).

[2] Liu, J.; Li, K.; Chen, Y.; Ding, H.; Wu, H.; Gao, Y.; Huang, S.; Wu, H.; Kong, D.; Yang, Z.; et al. Active and smart biomass film containing cinnamon oil and curcumin for meat preservation and freshness indicator. *Food Hydrocoll.* **2022**, *133*, https://doi.org/10.1016/j.foodhyd.2022.107979.

[3] Wang, X.; Fang, W.; Yan, D.; Han, D.; Liu, J.; Ren, Z.; Ouyang, C.; Li, Y.; Wang, Q.; Cao, A. Evaluation of the influence of temperature and relative humidity on the permeability of four films to the fumigant dimethyl disulfide. *J. Environ. Manag.* **2019**, *236*, 687–694, https://doi.org/10.1016/j.jenvman.2018.12.075.

[4] Dilkes-Hoffman, L.S.; Pratt, S.; Laycock, B.; Ashworth, P.; Lant, P.A. Public attitudes towards plastics. *Resour. Conserv. Recycl.* **2019**, *147*, 227–235, https://doi.org/10.1016/j.resconrec.2019.05.005.

[5] Duan, C.; Fang, Y.; Sun, J.; Li, Z.; Wang, Q.; Bai, J.; Peng, H.; Liang, J.; Gao, Z. Effects of fast food packaging plasticizers and their metabolites on steroid hormone synthesis in H295R cells. *Sci. Total. Environ.* **2020**, *726*, 138500, https://doi.org/10.1016/j.scitotenv.2020.138500.

[6] K. Marsh et B. Bugusu, Food packaging—Roles, materials, and environmental issues, Journal of Food Science,, 72 (2007) R39-R55.

[7] Han, Y.; Ding, J.; Zhang, J.; Li, Q.; Yang, H.; Sun, T.; Li, H. Fabrication and characterization of polylactic acid coaxial antibacterial nanofibers embedded with cinnamaldehyde/tea polyphenol with food packaging potential. *Int. J. Biol. Macromol.* **2021**, *184*, 739–749, https://doi.org/10.1016/j.ijbiomac.2021.06.143.

[8] Thiviya, P.; Gamage, A.; Liyanapathiranage, A.; Makehelwala, M.; Dassanayake, R.; Manamperi, A.; Merah, O.; Mani, S.; Koduru, J.R.; Madhujith, T. Algal polysaccharides: Structure, preparation and applications in food packaging. *Food Chem.* **2023**, *405*, https://doi.org/10.1016/j.foodchem.2022.134903.

[9] S. Sunanda et B. B. Khatua, Synthesis of Highly Exfoliated PS/Na+-MMTNanocomposites by Suspension Polymerization Using Na+-MMT Clay Platelets as Suspension Stabilizer, Macromolecular Research, 19 (2011) 44-52.

[10] Mostafavi, F.S.; Zaeim, D. Agar-based edible films for food packaging applications—A review. *Int. J. Biol. Macromol.* **2020**, *159*, 1165–1176, doi:10.1016/j.ijbiomac.2020.05.123.

[11] Y. Azuma, N. Yoshie, M. Sakurai, Y. Inoue et R. Chûjô, Thermal behaviour and miscibility of poly(3-hydroxybutyrate)/poly(vinyl alcohol) blends, Polymer, 33 (22) 4763-4767..

[12] Cahú, T.B.; Silva, R.A.; Silva, R.P.F.; Silva, M.M.; Arruda, I.R.S.; Silva, J.F.; Costa, R.M.P.B.; Santos, S.D.; Nader, H.B.; Bezerra, R.S. Evaluation of Chitosan-Based Films Containing Gelatin, Chondroitin 4-Sulfate and ZnO for Wound Healing. *Appl. Biochem. Biotechnol.* **2017**, *183*, 765–777, https://doi.org/10.1007/s12010-017-2462-z.

[13] J. Zhou, G. Romero, E. Rojas, L. Ma, S. Moya et C. Gao, Macromolecular Chemistry and Physics, 211 (2010) 377–484.

[14] S, H.; M, H.; M, A.; E, K. The effect of chitosan on physical and mechanical properties of paper. *J. Chem. Eng. Mater. Sci.* **2016**, *7*, 1–10, https://doi.org/10.5897/jcems2015.0235.

[15] S. K. Rout, Physicochemical, Functional and Spectroscopic analysis of crawfish chitin and chitosan as affected by process modification., Thèse de doctorat, 2001.

[16] Chen, S.; Zhang, Z.; Wei, X.; Sui, Z.; Geng, J.; Xiao, J.; Huang, D. Antibacterial and antioxidant water-degradable food packaging chitosan film prepared from American cockroach. *Food Biosci.* **2022**, *49*, https://doi.org/10.1016/j.fbio.2022.101893.

[17] P. Cazon et M. Vazquez, Applications of chitosan as food packaging materials. In Sustainable Agriculture Reviews book, 36 (2019) 81-12.

[18] Yu, Q.; Song, Y.; Shi, X.; Xu, C.; Bin, Y. Preparation and properties of chitosan derivative/poly(vinyl alcohol) blend film crosslinked with glutaraldehyde. *Carbohydr. Polym.* **2011**, *84*, 465–470, https://doi.org/10.1016/j.carbpol.2010.12.006.

[19] Narasagoudr, S.S.; Hegde, V.G.; Chougale, R.B.; Masti, S.P.; Dixit, S. Influence of boswellic acid on multifunctional properties of chitosan/poly (vinyl alcohol) films for active food packaging. *Int. J. Biol. Macromol.* **2020**, *154*, 48–61, https://doi.org/10.1016/j.ijbiomac.2020.03.073.

[20] Giannelis, E.P. A new strategy for synthesizing polymer-ceramic nanocomposites. *JOM* **1992**, *44*, 28–30, https://doi.org/10.1007/bf03222789.

[21] Y. Kojima, A. Usuki, M. Kawasumi, A. Okada et O. K. T. Karauchi, Sorption of water in nylon 6-clay hybrid(Article), J Polym Sci Part A, 49 (1993) 1259-1264.

[22] Li, Y.; Du, Q.; Liu, T.; Peng, X.; Wang, J.; Sun, J.; Wang, Y.; Wu, S.; Wang, Z.; Xia, Y.; et al. Comparative study of methylene blue dye adsorption onto activated carbon, graphene oxide, and carbon nanotubes. *Chem. Eng. Res. Des.* **2013**, *91*, 361–368, https://doi.org/10.1016/j.cherd.2012.07.007.

[23] Xiao, W.; Li, X.; Guo, H.; Wang, Z.; Zhang, Y.; Zhang, X. Preparation of core–shell structural single ionic conductor SiO2@Li+ and its application in PVDF–HFP-based composite polymer electrolyte. *Electrochimica Acta* **2012**, *85*, 612–621, https://doi.org/10.1016/j.electacta.2012.08.120.

[24] Li, C.; Hou, T.; Vongsvivut, J.; Li, Y.; She, X.; She, F.; Gao, W.; Kong, L. Simultaneous crystallization and decomposition of PVA/MMT composites during non-isothermal process. *Thermochim. Acta* **2015**, *618*, 26–35, https://doi.org/10.1016/j.tca.2015.09.009.

[25] Yeun, J.-H.; Bang, G.-S.; Park, B.J.; Ham, S.K.; Chang, J.-H. Poly(vinyl alcohol) nanocomposite films: Thermooptical properties, morphology, and gas permeability. *J. Appl. Polym. Sci.* **2006**, *101*, 591–596, https://doi.org/10.1002/app.23372.

[26] C. Grunlan, A. Grigorian, C. Hamilton et A. Mehrabi, Effect of clay concentration on the oxygen permeability and optical properties of a modified poly(vinyl alcohol), Journal of Applied Polymer Science, 93 (2004) 1102-1109.

[27] C. Thong, D. Teo et C. Ng, Application of polyvinyl alcohol (PVA) in cement-based composite materials: A review of its engineering properties and microstructure behavior., Constr. Build. Mater, 107 (2016) 172–180..

[28] Hoque, A.; Ahmed, M.; Rahman, G.; Islam, M.; Khan, M.A.; Hossain, M.K. Fabrication and comparative study of magnetic Fe and α-Fe2O3 nanoparticles dispersed hybrid polymer (PVA + Chitosan) novel nanocomposite film. *Results Phys.* **2018**, *10*, 434–443, https://doi.org/10.1016/j.rinp.2018.06.010.

[29] Y. Wang, Z. Zhou et Y. Han, Levan-chitosan blend films: Preparation, structural, physical properties and application in pork packaging, International Journal of Biological Macromolecules, 217 (2022) 624-632.

[30] Yang, J.; Shen, M.; Luo, Y.; Wu, T.; Wen, H.; Xie, J. Construction and characterization of Mesona chinensis polysaccharide-chitosan hydrogels, role of chitosan deacetylation degree. *Carbohydr. Polym.* **2021**, *257*, 117608, https://doi.org/10.1016/j.carbpol.2020.117608.

[31] Chen, J.-K.; Yeh, C.-H.; Wang, L.-C.; Liou, T.-H.; Shen, C.-R.; Liu, C.-L. Chitosan, the Marine Functional Food, Is a Potent Adsorbent of Humic Acid. *Mar. Drugs* **2011**, *9*, 2488–2498, https://doi.org/10.3390/md9122488.

[32] Zhang, W.; Shu, C.; Chen, Q.; Cao, J.; Jiang, W. The multi-layer film system improved the release and retention properties of cinnamon essential oil and its application as coating in inhibition to penicillium expansion of apple fruit. *Food Chem.* **2019**, *299*, 125109, https://doi.org/10.1016/j.foodchem.2019.125109.

[33] R. Priyadarshi et J. Rhim, Chitosan-based biodegradable functional films for food packaging applications, Innovative Food Science & Emerging Technologies, 62 (2020) 102346.

[34] Mouzahim, M.; Eddarai, E.; Eladaoui, S.; Guenbour, A.; Bellaouchou, A.; Zarrouk, A.; Boussen, R. Effect of Kaolin clay and Ficus carica mediated silver nanoparticles on chitosan food packaging film for fresh apple slice preservation. *Food Chem.* **2023**, *410*, 135470, https://doi.org/10.1016/j.foodchem.2023.135470.

[35] Zhang, W.; Jiang, W. Antioxidant and antibacterial chitosan film with tea polyphenols-mediated green synthesis silver nanoparticle via a novel one-pot method. *Int. J. Biol. Macromol.* **2019**, *155*, 1252–1261, https://doi.org/10.1016/j.ijbiomac.2019.11.093.

[36] Aam, B.B.; Heggset, E.B.; Norberg, A.L.; Sørlie, M.; Vårum, K.M.; Eijsink, V.G.H. Production of Chitooligosaccharides and Their Potential Applications in Medicine. *Mar. Drugs* **2010**, *8*, 1482–1517, https://doi.org/10.3390/md8051482.

[37] Shen, C.-R.; Wu, S.-T.; Tsai, Z.-T.; Wang, J.-J.; Yen, T.-C.; Tsai, J.-S.; Shih, M.-F.; Liu, C.-L. Characterization of quaternized chitosan-stabilized iron oxide nanoparticles as a novel potential magnetic resonance imaging contrast agent for cell tracking. *Polym. Int.* **2011**, *60*, 945–950, https://doi.org/10.1002/pi.3059.

[38] k. Sushil et D. K. Aswal, Recent Advances in Thin Film book: Thin Film and Significance of Its Thickness chapter, (2020) 1–12.

[39] F. B. Dhieb, E. J. Dil, S. H. Tabatabaei, F. Mighri et A. Ajji, Effect of nanoclay orientation on oxygen barrier properties of LbL nanocomposite coated films, RSC Advances, 9 (2019) 1632–1641.

[40] Torres-Huerta, A.; Palma-Ramírez, D.; Domínguez-Crespo, M.; Del Angel-López, D.; de la Fuente, D. Comparative assessment of miscibility and degradability on PET/PLA and PET/chitosan blends. *Eur. Polym. J.* **2014**, *61*, 285–299, https://doi.org/10.1016/j.eurpolymj.2014.10.016.

[41] Masood, F.; Ain, N.U.; Habib, S.; Alam, A.; Yasin, T.; Hameed, A.; Farooq, M. Preparation, characterization, and evaluation of multifunctional properties of PVA/metal oxide@sepiolite nanocomposite membranes for water cleanup. *Mater. Today Commun.* **2022**, *31*, https://doi.org/10.1016/j.mtcomm.2022.103620.

[42] Z. Yu, B. Li, J. Chu et P. Zhang, In Situ Silica Reinforced PVA/Chitosan Biodegradable Films for Food Packaging, Carbohydrate Polymers, 184 (2018) 214 - 220.

[43] N. Zainuddin et A. Samsudin, Investigation on the effect of NH4Br at transport properties in K–carrageenan-based biopolymer electrolytes via structural and electrical analysis, Mater. Today Commun., 14 (2018) 199-209.

[44] Ranjana, R.; Parushuram, N.; Harisha, K.S.; Asha, S.; Narayana, B.; Mahendra, M.; Sangappa, Y. Fabrication and characterization of conductive silk fibroin–gold nanocomposite films. *J. Mater. Sci. Mater. Electron.* **2019**, *31*, 249–264, https://doi.org/10.1007/s10854-019-02485-5.

[45] P. Wei, ACS Sustain. Chem. Eng., 7 (2019) 1707-1717.

[46] L. Mao, J. Y. Z. Bai et Y. Liu, Development of novel poly(lactic acid) active multilayer composite films by incorporating catechol-functionalized layered clay into chitosan/poly(vinyl alcohol) coatings, Progress in Organic Coatings, 170 (2022) 107000.

[47] Barnabeo, A.E.; Creasy, W.S.; Robeson, L.M. Gas permeability characteristics of nitrile-containing block and random copolymers. *J. Polym. Sci. Polym. Chem. Ed.* **1975**, *13*, 1979–1986, https://doi.org/10.1002/pol.1975.170130902.

[48] N. Peppas et E. Merrill, Differential scanning calorimetry of crystalline PVA hydrogels., Journal of Applied Polymer Science,, 20 (1976) 1457-1465.

[49] O. G. Abdullah, S. Aziz et M. Rasheed, Structural and optical characterization of PVA: KMnO4 based solid polymer electrolyte, Results in Physics, 6 (2016) 1103-1108.

[50] Zamani, M.; Gholibegloo, E.; Aghajanzadeh, M.; Salehian, F.; Ebrahimi, S.E.S.; Ganjali, M.R.; Mahdavi, H.; Khoobi, M. Polyvinyl alcohol-graphene oxide nanocomposites: evaluation of flame-retardancy, thermal and mechanical properties. *J. Macromol. Sci. Part A* **2019**, *57*, 17–24, https://doi.org/10.1080/10601325.2019.1578617.

[51] Strenkoski, M.; Wlodarczyk, D.; Piszczyk, L.; Strankowska, J. Polyurethane Nanocomposites Containing Reduced Graphene Oxide, FTIR, Raman, and XRD Studies. *J. Spectrosc.* **2016**, *2016*, 7520741, doi:10.1155/2016/7520741.

[52] M. R. Khan, S. Pal, M. Hoque, M. Alam, M. Younus et H. Kobayashi, Simple fabrication of PVA-ZnS composite films with superior photocatalytic performance: enhanced luminescence property, morphology, and thermal stability, ACS Omega, 4 (2019) 6144-6153.

[53] K. C. Mruthyunjayappa, S. A. Paramashivaiah, E. K. Mallikarjunappa, S. M. Padre, S. Gurumurthy, S. Surabhi, J.-R. Jeong, D. V. M. Montecinos et M. S. Murari, A combined experimental and computational study of flexible polyvinyl alcohol (PVA)/graphene oxide (GO) nanocomposite films for superior UV shielding with improved mechanical properties, Materials Today Communications, 35 (2023) article 105662.

[54] Kasai, D.; Chougale, R.; Masti, S.; Gouripur, G.; Malabadi, R.; Chalannavar, R.; Raghu, A.V.; Radhika, D.; H., S.; Dhanavant, S. Preparation, characterization and antimicrobial activity of betel-leaf-extract-doped polysaccharide blend films. *Green Mater.* **2021**, *9*, 49–68, https://doi.org/10.1680/jgrma.20.00014.

[55] A. Elbarbary et N. El-Sawy, Radiation synthesis and characterization of polyvinyl alcohol/chitosan/silver nanocomposite membranes: antimicrobial and blood compatibility studies, Polym. Bull., 74 (2017) 195-212.

[56] Falqi, F.H.; Bin-Dahman, O.A.; Hussain, M.; Al-Harthi, M.A. Preparation of Miscible PVA/PEG Blends and Effect of Graphene Concentration on Thermal, Crystallization, Morphological, and Mechanical Properties of PVA/PEG (10 wt%) Blend. *Int. J. Polym. Sci.* **2018**, *2018*, 1–10, https://doi.org/10.1155/2018/8527693.

[57] Wang, H.; Gong, X.; Miao, Y.; Guo, X.; Liu, C.; Fan, Y.-Y.; Zhang, J.; Niu, B.; Li, W. Preparation and characterization of multilayer films composed of chitosan, sodium alginate and carboxymethyl chitosan-ZnO nanoparticles. *Food Chem.* **2019**, *283*, 397–403, https://doi.org/10.1016/j.foodchem.2019.01.022.

[58] L. Deng, H. Qi, C. Yao, M. Feng et A. Dong, Investigation on the properties of methoxy poly (ethylene glycol)/chitosan graft co-polymers, Solid State Ionics, 18 (2012) 1575-1589.

[59] R. Charles et K. Varun, Degradation of polyvinyl Alcohol in Wastewater treatment Plants and Subsequent Nationwide Emission Estimate, International Journal of Environmental Research and Public Health , 18 (2021), 6027.

[60] H. C. Y. L. S.Y. Nam, Pervaporation Separation of Water-Isopropanol Mixture Using Carboxymethylated Poly(vinyl alcohol) Composite Membranes, J. Appl. Polym. Sci.,, vol. 72, pp. 241-249, 1999.

[61] J. L. Holloway, A. M. Lowman et G. R. Palmese, The role of crystallization and phase separation in the formation of physically cross-linked PVA hydrogels, hydrogels Soft Matter, 9 (2013) 826-83.

[62] Zhu, K.; Duan, J.; Guo, J.; Wu, S.; Lu, A.; Zhang, L. High-Strength Films Consisted of Oriented Chitosan Nanofibers for Guiding Cell Growth. *Biomacromolecules* **2017**, *18*, 3904–3912, https://doi.org/10.1021/acs.biomac.7b00936.

[63] Naito, P.-K.; Ogawa, Y.; Kimura, S.; Iwata, T.; Wada, M. Crystal transition from hydrated chitosan and chitosan/monocarboxylic acid complex to anhydrous chitosan investigated by X-ray diffraction. *J. Polym. Sci. Part B: Polym. Phys.* **2015**, *53*, 1065–1069, https://doi.org/10.1002/polb.23748.

[64] Hua, M.; Wu, S.; Ma, Y.; Zhao, Y.; Chen, Z.; Frenkel, I.; Strzalka, J.; Zhou, H.; Zhu, X.; He, X. Strong tough hydrogels via the synergy of freeze-casting and salting out. *Nature* **2021**, *590*, 594–599, https://doi.org/10.1038/s41586-021-03212-z.

[65] Chen, Y.; Zhang, Q.; Zhong, Y.; Wei, P.; Yu, X.; Huang, J.; Cai, J. Super-Strong and Super-Stiff Chitosan Filaments with Highly Ordered Hierarchical Structure. *Adv. Funct. Mater.* **2021**, *31*, 2104368, https://doi.org/10.1002/adfm.202104368.

[66] M. Mredha, Y. Z. Guo, T. Nonoyama, T. Nakajima, T. Kurokawa et J. P. Gong, A Facile Method to Fabricate Anisotropic Hydrogels with Perfectly Aligned Hierarchical Fibrous Structures, Adv. Mater.,, 30 (2018) 1704937.

[67] F. G. Alabarse, R. V. Conceição, N. M. Balzaretti, F. Schenato et A. M. Xavier, Analyses FTIR in-situ de la bentonite sous haute pression, Appl. Argile Sci., 51 (2011) 202 - 208.

[68] Krupskaya, V.V.; Zakusin, S.V.; Tyupina, E.A.; Dorzhieva, O.V.; Zhukhlistov, A.P.; Belousov, P.E.; Timofeeva, M.N. Experimental Study of Montmorillonite Structure and Transformation of Its Properties under Treatment with Inorganic Acid Solutions. *Minerals* **2017**, *7*, 49, https://doi.org/10.3390/min7040049.

[69] J. Hizal, M. Yilmazoglu, N. Kanmaz et E. Ercag, Efficient removal of indigo dye by using sulfonated poly (ether ketone) (sPEEK), montmorillonite (MMT) and sPEEK-MMT composites as novel adsorbent, Chemical, Physics Letters, 794 (2022) 139482.

[70] S. Liu, P. Cai, X. Li, L. Chen, L. Li et B. Li, Effect of film multi-scale structure on the water vapor permeability in hydroxypropyl starch (HPS)/Na-MMT nanocomposites, Carbohydrate Polymers, 154 (2016) 186-193.

[71] K. Sermsantiwanit et S. Phattanaruedee, Preparation of bio-based nanocomposite emulsions: Effect of clay type, Progress in Organic Coatings, 74 (2012) 660-666.

[72] Alboofetileh, M.; Rezaei, M.; Hosseini, H.; Abdollahi, M. Effect of montmorillonite clay and biopolymer concentration on the physical and mechanical properties of alginate nanocomposite films. *J. Food Eng.* **2013**, *117*, 26–33, https://doi.org/10.1016/j.jfoodeng.2013.01.042.

[73] Vilela, S.O.; Soto-Oviedo, M.A.; Albers, A.P.F.; Faez, R. Polyaniline and mineral clay-based conductive composites. *Mater. Res.* **2007**, *10*, 297–300, https://doi.org/10.1590/s1516-14392007000300015.

[74] Mathew, S.; Snigdha, S.; Mathew, J.; Radhakrishnan, E. Poly(vinyl alcohol): Montmorillonite: Boiled rice water (starch) blend film reinforced with silver nanoparticles; characterization and antibacterial properties. *Appl. Clay Sci.* **2018**, *161*, 464–473, https://doi.org/10.1016/j.clay.2018.05.009.

[75] M. Dinari et A. Nabiyan, Citric acid-modified layered double hydroxide as a green reinforcing agent for improving thermal properties, Polym. Compos., 37 (2016) 1-9.

[76] Chen, B.; Evans, J.R.G.; Greenwell, H.C.; Boulet, P.; Coveney, P.V.; Bowden, A.A.; Whiting, A. A critical appraisal of polymer–clay nanocomposites. *Chem. Soc. Rev.* **2007**, *37*, 568–594, https://doi.org/10.1039/b702653f.

[77] L. W. A. W. J. Zhang, Preparation and Properties of Chitosan-g-poly(acrylic acid)/Montmorillonite Superabsorbent Nanocomposite via in Situ Intercalative Polymerization, Ind. Eng. Chem. Res., 46 (2007) 2497-2502.

[78] Pulikkalparambil, H.; Varghese, S.A.; Siengchin, S.; Parameswaranpillai, J. Thermally mendable and improved hydrophilic bioepoxy/PEG-PPG-PEG blends for coating application. *Mater. Res. Express* **2018**, *6*, 025307, https://doi.org/10.1088/2053-1591/aaeccf.

[79] Jayaraju, J.; Keshavayya, J.; Rai, S.K.; Basavaraju, K.C. Miscibility Studies on Chitosan/Poly(vinyl alcohol) Blends. *J. Macromol. Sci. Part A* **2008**, *45*, 271–275, https://doi.org/10.1080/10601320701863684.

[80] R. J. Ashley, Permeability and plastics packaping, J. Comyn (Ed.), Polymer permeability, (1985) 269-308.

[81] LaChance, A.M.; Hou, Z.; Farooqui, M.M.; Samuels, N.T.; Carr, S.A.; Serrano, J.M.; Odendahl, C.E.; Hurley, M.E.; Morrison, T.E.; Kubachka, J.L.; et al. Spin Coating for Forming Thin Composite Coatings of Montmorillonite and Poly(vinyl alcohol). *Ind. Eng. Chem. Res.* **2022**, *61*, 4168–4177, https://doi.org/10.1021/acs.iecr.1c04382.